

Ángel R. Landa-Cánovas,^{a*}
Eladio Vila,^a Jorge Hernández-
Velasco,^a Jean Galy^b and Alicia
Castro^a

^aInstituto de Ciencia de Materiales de Madrid, ICMM, CSIC, Sor Juana Inés de la Cruz 3, Cantoblanco, 28049 Madrid, Spain, and ^bCentre d'Elaboration de Matériaux et d'Etudes Structurales CNRS, 29 rue Jeanne Marvig, BP 94347, 31055 Toulouse CEDEX 4, France

Correspondence e-mail: landa@icmm.csic.es

Structural elucidation of the $\text{Bi}_{2(n+2)}\text{Mo}_n\text{O}_{6(n+1)}$ ($n = 3, 4, 5$ and 6) family of fluorite superstructures by transmission electron microscopy

Received 4 May 2009
Accepted 22 June 2009

The cationic framework structure of a whole new family of compounds with the general formula $\text{Bi}_{2(n+2)}\text{Mo}_n\text{O}_{6(n+1)}$ ($n = 3, 4, 5$ and 6) has been elucidated by transmission electron microscopy (TEM) methods. High-resolution transmission electron microscopy (HRTEM) has been used to postulate heavy-atom models based on the known structure of the $n = 3$ phase, $\text{Bi}_{10}\text{Mo}_3\text{O}_{24}$. These models were tested by HRTEM image simulation, electron diffraction and powder X-ray diffraction simulation methods which agreed with the experimental results. The four known phases of this family correspond to $n = 3, 4, 5$ and 6 members and all show fluorite superstructures. They consist of a common $\delta\text{-Bi}_2\text{O}_3$ fluorite-type framework, inside of which are distributed ribbons of $\{\text{MoO}_4\}$ tetrahedra which are infinite along **b**, one tetrahedron thick along **c**, and of variable widths of 3, 4, 5 or 6 $\{\text{MoO}_4\}$ tetrahedra along **a** depending on the family member (n value). These $\{\text{MoO}_4\}$ tetrahedra are isolated, *i.e.* without sharing any corner as in the $[\text{Bi}_{12}\text{O}_{14}]$ columnar structural-type phase $\text{Bi}[\text{Bi}_{12}\text{O}_{14}][\text{MoO}_4]_4[\text{VO}_4]$. The structure of all these family members can be described as crystallographic shear derivatives from Aurivillius-type phases such as Bi_2MoO_6 , the $n = \infty$ end member. All these compounds are good oxygen-ion conductors.

1. Introduction

$\delta\text{-Bi}_2\text{O}_3$, a material with a fluorite-type structure, is one of the best solid-state oxygen-ion conductors. It is a high-temperature form that cannot be quenched to room temperature. However, doping with small amounts of transition metal oxides preserves the $\delta\text{-Bi}_2\text{O}_3$ structure at low temperature and retains its anionic conduction properties. There are new families of oxygen conductors structurally related to the fluorite framework in such systems as $\text{Bi}_2\text{O}_3\text{-V}_2\text{O}_5$, $\text{Bi}_2\text{O}_3\text{-Ta}_2\text{O}_5$ and $\text{Bi}_2\text{O}_3\text{-Nb}_2\text{O}_5$ (Roth & Waring, 1962; Zhou *et al.*, 1987; Miida & Tanaka, 1990). In these systems the Bi_2O_3 -rich ends always show fluorite-type superstructures (Ling *et al.*, 1998; Castro *et al.*, 1998; Castro & Palem, 2002; Ling, 1999; Pirnat *et al.*, 2005).

The $\text{Bi}_2\text{O}_3\text{-MoO}_3$ materials are interesting because of their functional properties, chiefly as catalysts (Brazdil *et al.*, 1980; Galvan *et al.*, 1993; Agarwal *et al.*, 1994) and also as good ionic conductors (Bégué *et al.*, 1998; Vannier *et al.*, 1999, 2000; Grins *et al.*, 2002; Bégué *et al.*, 2002; Bastide *et al.*, 2003; Duc *et al.*, 2004; Galy *et al.*, 2006; Mukhta & Guru Row, 2007; Holmes *et al.*, 2008; Vera & Aragón, 2008). All the phases in this system are related to the fluorite structure (Crumpton *et al.*, 2003; Valldor *et al.*, 2000; Buttrey *et al.*, 1986*a,b*; Spinolo & Tomasi, 1997; Kohlmüller & Badaud, 1969; Buttrey *et al.*, 1997; Enjalbert *et al.*, 1997; Chen & Sleight, 1986; Theobald *et al.*,

Table 1

 Cationic structural model proposed for $\text{Bi}_{10}\text{Mo}_3\text{O}_{24}$.

 $a = 23.7235$ (4), $b = 5.64720$ (8) and $c = 8.6798$ (1) Å and $\beta = 95.879$ (1)° (at room temperature); space group $C2$.

	<i>x</i>	<i>y</i>	<i>z</i>
Mo1	0.0	0.0	0.0
Mo2	23/26	0.5	1/13
Bi1	20/26	0.0	2/13
Bi2	17/26	0.5	3/13
Bi3	14/26	0.0	4/13
Bi4	11/26	0.5	5/13
Bi5	8/26	0.0	6/13

1985), except Bi_2MoO_6 [γ (L)-phase $\text{Bi}_{10}\text{Mo}_3\text{O}_{24}$] which shows an Aurivillius-type structure (Buttrey *et al.*, 1994).

Recently, the authors have reported the preparation of new phases in the Bi–Mo–O system prepared by synthesis methods alternative to the ceramic method, like soft-wet chemistry methods, which allow the isolation of low-temperature phases. A whole new family of low-temperature phases $\text{Bi}_{2(n+2)}\text{Mo}_n\text{O}_{6(n+1)}$, namely $n = 3$ ($\text{Bi}_{10}\text{Mo}_3\text{O}_{24}$), $n = 4$ ($\text{Bi}_{12}\text{Mo}_4\text{O}_{30}$), $n = 5$ ($\text{Bi}_{14}\text{Mo}_5\text{O}_{36}$) and $n = 6$ ($\text{Bi}_{16}\text{Mo}_6\text{O}_{42}$; Vila *et al.*, 2004, 2005, 2007). The Bi/Mo ratios are 3.33 ($n = 3$), 3.0 ($n = 4$), 2.8 ($n = 5$) and 2.66 ($n = 6$). The two Bi-rich phases were suggested to be related to the so-called $[\text{Bi}_{12}\text{O}_{14}]$ columnar structural type by Vila *et al.* (2004, 2005), as with the $\text{Bi}[\text{Bi}_{12}\text{O}_{14}][\text{MoO}_4]_4[\text{VO}_4]$ phase in the Bi–Mo–V–O system, see Enjalbert *et al.* (1997).

All these compounds have been demonstrated to be closely structurally related by electron diffraction methods combined with powder X-ray diffraction (Vila *et al.*, 2007), showing that the four studied phases are members of a homologous series of phases whose reciprocal lattices can be described as conse-

Table 2

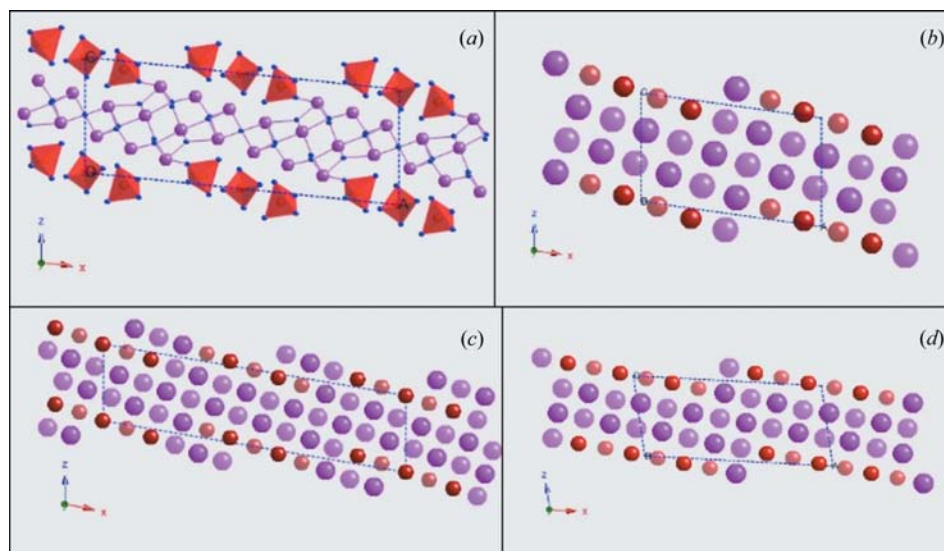
 Cationic structural model proposed for $\text{Bi}_{12}\text{Mo}_4\text{O}_{30}$.

 $a = 14.5337$ (4), $b = 5.64795$ (7) and $c = 8.6620$ (1) Å and $\beta = 97.979$ (1)° (at room temperature); space group $P2_1$.

	<i>x</i>	<i>y</i>	<i>z</i>
Mo1	29/32	0.0	1/32
Mo2	23/32	0.5	3/32
Bi1	17/32	0.0	5/32
Bi2	11/32	0.5	7/32
Bi3	5/32	0.0	9/32
Bi4	31/32	0.5	11/32
Bi5	25/32	0.0	13/32
Bi6	19/32	0.5	15/32

cutive superstructures of the basic $\delta\text{-Bi}_2\text{O}_3$ fluorite subcell. However, no atomic model was proposed for the structure of these fluorite superstructures. The conductor behaviour of these materials was also studied and compared; impedance spectroscopy measurements showed that these materials are quite good ionic conductors. Very recently Galy *et al.* (2009) solved and refined the structure of $\text{Bi}_{10}\text{Mo}_3\text{O}_{24}$ by a combination of high-resolution transmission electron microscopy (HRTEM) and powder X-ray and neutron diffraction methods. The structure of $\text{Bi}_{10}\text{Mo}_3\text{O}_{24}$ is described as consisting of $[\text{Bi}_{10}\text{O}_{12}]$ puckered layers running parallel to the (001) plane and sandwiching groups of three isolated $\{\text{MoO}_4\}$ tetrahedra, see Fig. 1(a).

This work deals with the elucidation of the crystal structures of all these related phases mainly from HRTEM supported by selected-area electron diffraction. The rest of the paper is organized as follows: §2 contains the technical details on the preparation of the samples and technical aspects of the char-


Figure 1

(a) Structure model of $\text{Bi}_{10}\text{Mo}_3\text{O}_{24}$ refined by simultaneous X-ray and neutron powder diffraction (Galy *et al.*, 2009). (b) Heavy-atom skeleton model proposed for the $n = 4$ phase, $\text{Bi}_{12}\text{Mo}_4\text{O}_{30}$. (c) Heavy-atom skeleton model proposed for the $n = 5$ phase, $\text{Bi}_{14}\text{Mo}_5\text{O}_{36}$. (d) Heavy-atom skeleton model proposed for the $n = 6$ phase, $\text{Bi}_{16}\text{Mo}_6\text{O}_{42}$. Blue spheres denote oxygen, purple ones bismuth and red molybdenum. The different shades of Mo and Bi atoms indicate heights of 0 and $\frac{1}{2}$.

acterization techniques employed. In §3 we first describe in detail the TEM characterization of the $\text{Bi}_{10}\text{Mo}_3\text{O}_{24}$ phase and how a cationic model derived from Galy *et al.*'s (2009) structure refinements can be used to calculate HRTEM image simulations which are compared with HRTEM experimental images and with electron diffraction and powder X-ray diffraction simulations. Following this procedure HRTEM images were used to derive cationic structure models for the remaining low-temperature phases: $\text{Bi}_{12}\text{Mo}_4\text{O}_{30}$, $\text{Bi}_{14}\text{Mo}_5\text{O}_{36}$ and $\text{Bi}_{16}\text{Mo}_6\text{O}_{42}$; models which were validated through multislice image simulations. Finally, a structural discussion relates the structures

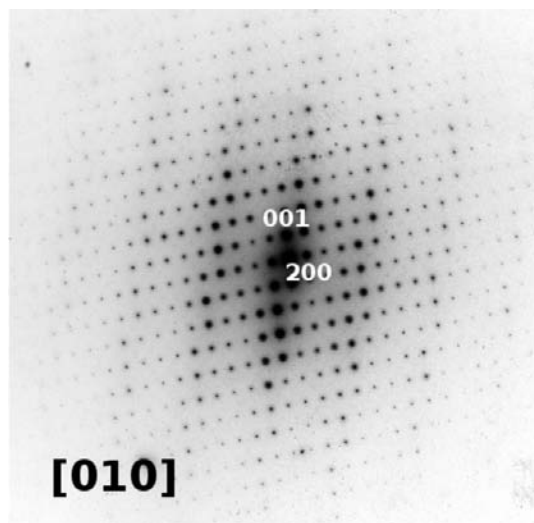


Figure 2
SAED pattern of the $\text{Bi}_{10}\text{Mo}_3\text{O}_{24}$ phase oriented along the main $[010]$ direction. Note the intense fluorite sublattice reflections and the weaker superlattice reflections.

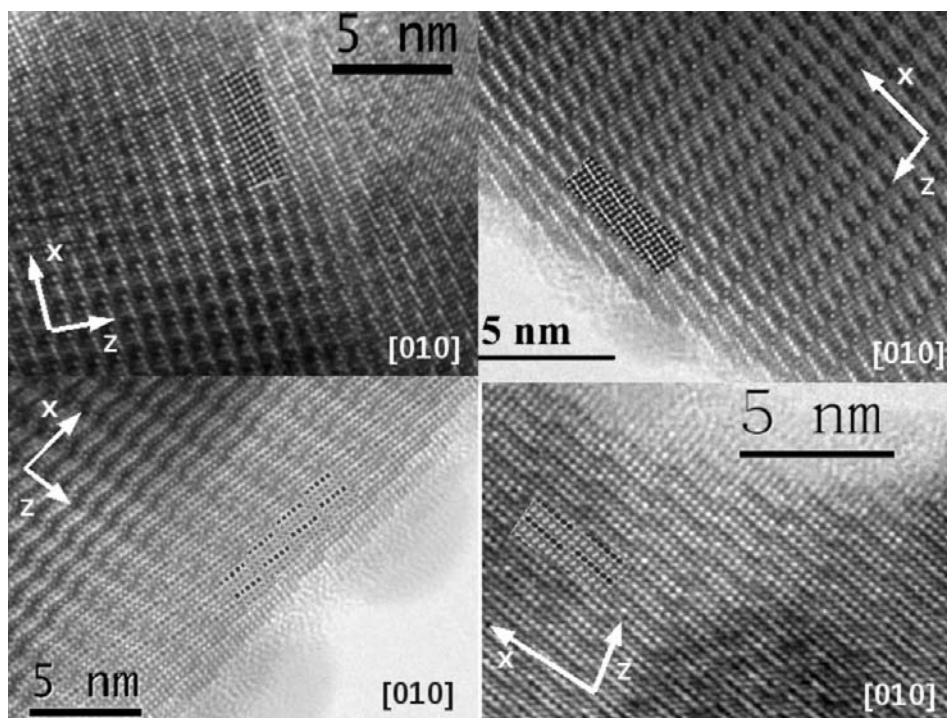


Figure 3
(a) High-magnification micrograph of an experimental HRTEM image of the $n = 3$ phase $\text{Bi}_{10}\text{Mo}_3\text{O}_{24}$. The simulated image in the center is for the cationic model derived from the structure model of Fig. 1(a), see Table 1, calculated for a defocus of -100 nm and a thickness of 10 nm. (b) HRTEM micrograph of a crystal of the $n = 4$ phase $\text{Bi}_{12}\text{Mo}_4\text{O}_{30}$. A simulated image is included with a thickness of 5 nm and a defocus of -60 nm for the cationic model proposed, whose atomic coordinates are collected in Table 2. (c) HRTEM micrograph of a crystal of the $n = 5$ phase $\text{Bi}_{14}\text{Mo}_5\text{O}_{36}$. A simulated image is included with a thickness of 5 nm and a defocus of -30 nm for the cationic model proposed, whose atomic coordinates are collected in Table 3. (d) HRTEM micrograph of a crystal of the $n = 6$ phase $\text{Bi}_{16}\text{Mo}_6\text{O}_{42}$. A simulated image is included with a thickness of 10 nm and a defocus of -20 nm for the cationic model proposed, whose atomic coordinates are collected in Table 4.

of these compounds with Bi_2MoO_6 and Aurivillius-type structure by means of crystallographic shear operations.

2. Experimental details

The so-called n -butylamine procedure, previously reported by Vila *et al.* (2004, 2005, 2007), has been used to synthesize the four low-temperature $\text{Bi}_{2(n+2)}\text{Mo}_n\text{O}_{6(n+1)}$ pure phases, with $n = 3$ ($\text{Bi}_{10}\text{Mo}_3\text{O}_{24}$), $n = 4$ ($\text{Bi}_{12}\text{Mo}_4\text{O}_{30}$), $n = 5$ ($\text{Bi}_{14}\text{Mo}_5\text{O}_{36}$) and $n = 6$ ($\text{Bi}_{16}\text{Mo}_6\text{O}_{42}$), *i.e.* for $m\text{Bi}_2\text{O}_3$ – MoO_3 compositions ranging from $m = 1.3$ to 1.7.

Powder X-ray diffraction experiments were carried out using a Philips X'Pert diffractometer, fitted with a Ge(111) incident-beam monochromator of the Johansson symmetric type, using $\text{Cu K}\alpha_1$ radiation ($\lambda = 1.54059 \text{ \AA}$). Data were recorded between 5 and 70° (2θ), with 2θ increments of 0.01° and a counting time of 20 s per step.

The single phases $\text{Bi}_{16}\text{Mo}_6\text{O}_{42}$, $\text{Bi}_{14}\text{Mo}_5\text{O}_{36}$, $\text{Bi}_{12}\text{Mo}_4\text{O}_{30}$ and $\text{Bi}_{10}\text{Mo}_3\text{O}_{24}$ were studied by transmission electron microscopy. Specimens for TEM observations were prepared from suspensions ultrasonically dispersed in butanol. A drop of each corresponding suspension was placed on a copper grid

covered with a holey carbon film. A JEM 2000FXII (ICMM) electron microscope was employed to explore the reciprocal lattices of the samples (double-tilt specimen holder: $\pm 45^\circ$) and to obtain medium-resolution images. HRTEM was carried out using a field-emission Jeol 3000F transmission electron microscope (from the Centro de Microscopía 'Luis Brú', Universidad Complutense de Madrid) with 1.7 \AA resolution. Image processing was carried out using *DigitalMicrograph* software distributed by Gatan. HRTEM image simulations were performed with NCEMSS software and electron diffraction and powder X-ray diffraction simulations were performed with the software package *CystalMaker*[®].

3. Results

3.1. The $n = 3$ phase, $\text{Bi}_{10}\text{Mo}_3\text{O}_{24}$

From the unit-cell parameters and from the relationships given by Vila *et al.* (2007), the simplest phase is the $n = 3$ member, *i.e.* $\text{Bi}_{10}\text{Mo}_3\text{O}_{24}$, with a Bi/Mo ratio

Table 3

 Cationic structural model proposed for $\text{Bi}_{14}\text{Mo}_5\text{O}_{36}$.

 $a = 34.476$ (2), $b = 5.6414$ (3) and $c = 8.6433$ (4) Å and $\beta = 99.690$ (5)° (at room temperature); space group $C2$.

	x	y	z
Mo1	0.0	0.0	0.0
Mo2	35/38	0.5	1/19
Mo3	32/38	0.0	2/19
Mo4	29/38	0.5	3/19
Bi1	26/38	0.0	4/19
Bi2	23/38	0.5	5/19
Bi3	20/38	0.0	6/19
Bi4	17/38	0.5	7/19
Bi5	14/38	0.0	8/19
Bi6	11/38	0.5	9/19
Bi7	8/38	0.0	10/19

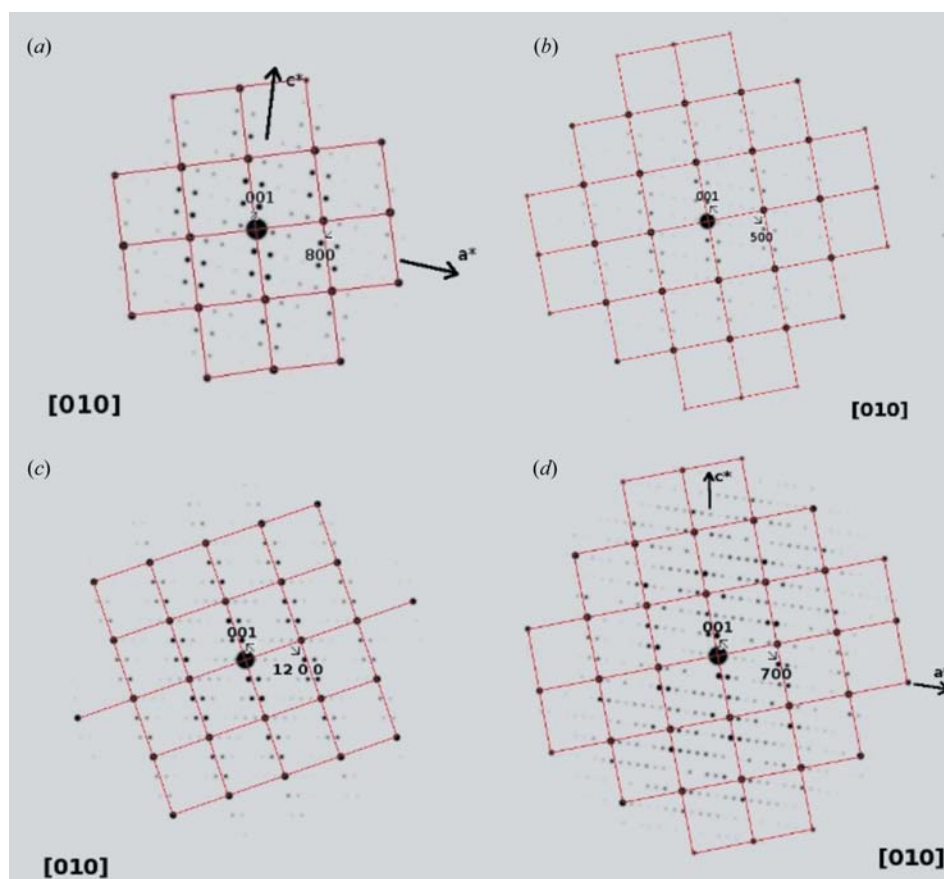
 of 3.33 and unit-cell parameters $a = 23.7235$ (4), $b = 5.64720$ (8) and $c = 8.6798$ (1) Å and $\beta = 95.879$ (1)°.

 Fig. 2 shows the most characteristic selected-area electron diffraction (SAED) pattern of the $\text{Bi}_{10}\text{Mo}_3\text{O}_{24}$ phase, oriented

 along the short axis, *i.e.* on the a^*c^* plane. The more intense reflections are related to the basic fluorite structure and the weak ones indicate a fluorite superstructure according to the following relationship given by Vila *et al.* (2005)

$$\begin{pmatrix} \mathbf{a}_M \\ \mathbf{b}_M \\ \mathbf{c}_M \end{pmatrix} = \begin{pmatrix} n+1 & 0 & 1 \\ 0 & 1 & 0 \\ -1/2 & 0 & 3/2 \end{pmatrix} \begin{pmatrix} \mathbf{a}_F \\ \mathbf{b}_F \\ \mathbf{c}_F \end{pmatrix}. \quad (1)$$

 The indexing of SAED patterns, oriented along different directions, agrees with the C-centering of the cell refined by Galy *et al.* (2009).

 Reasonably good quality HRTEM images could be obtained for the $\text{Bi}_{10}\text{Mo}_3\text{O}_{24}$ phase, see Fig. 3(a), in spite of the tendency of the crystals to decompose under the electron beam, producing small crystallites of Bi_2O_3 that are rapidly observed on the edge of the crystals, conditioning to work in low-dose conditions. The image clearly shows a well ordered crystal and consists of a regular array of straight segments composed of five intense white spots. These lines are arranged in a zigzag arrangement leaving two rows of weaker white spots in between. The basic fluorite subcell would consist of the simple square traced by the four closest white spots. The edge of the crystal is decorated by beam-radiation decomposition products like Bi_2O_3 nanocrystals. The thinner areas of the crystal at the edge cannot be used to obtain HRTEM images good enough for a 'weak phase object' (WPO) approximation, which would allow a direct intuitive interpretation of the image. Starting from a cationic model elucidated from HRTEM observations, we have recently refined the structure model and oxygen positions using simultaneous Rietveld refinements of multi-patterned X-ray and neutron powder diffraction data (Galy *et al.*, 2009). The complete refined model is shown in Fig. 1(a). The cationic framework of this structure was used to simulate the HRTEM which fitted very well with the experimental HRTEM image, see Fig. 3(a). Image simulations confirm that the oxygen anion sublattice is irrelevant to the HRTEM image contrast owing to the higher average Z value of the cationic sublattice. The

Figure 4

 SAED patterns simulated for the cationic model proposed for the $\text{Bi}_{10}\text{Mo}_3\text{O}_{24}$ phase (a), whose atomic coordinates are collected in Table 1, for the cationic model proposed for $\text{Bi}_{12}\text{Mo}_4\text{O}_{30}$ phase (b), Table 2, for the cationic model proposed for $\text{Bi}_{14}\text{Mo}_5\text{O}_{36}$ phase (c), Table 3, and for the cationic model proposed for $\text{Bi}_{16}\text{Mo}_6\text{O}_{42}$ phase (d), Table 4. The basic fluorite sublattice has been outlined in red. The indexed reflections refer to the fluorite superstructures.

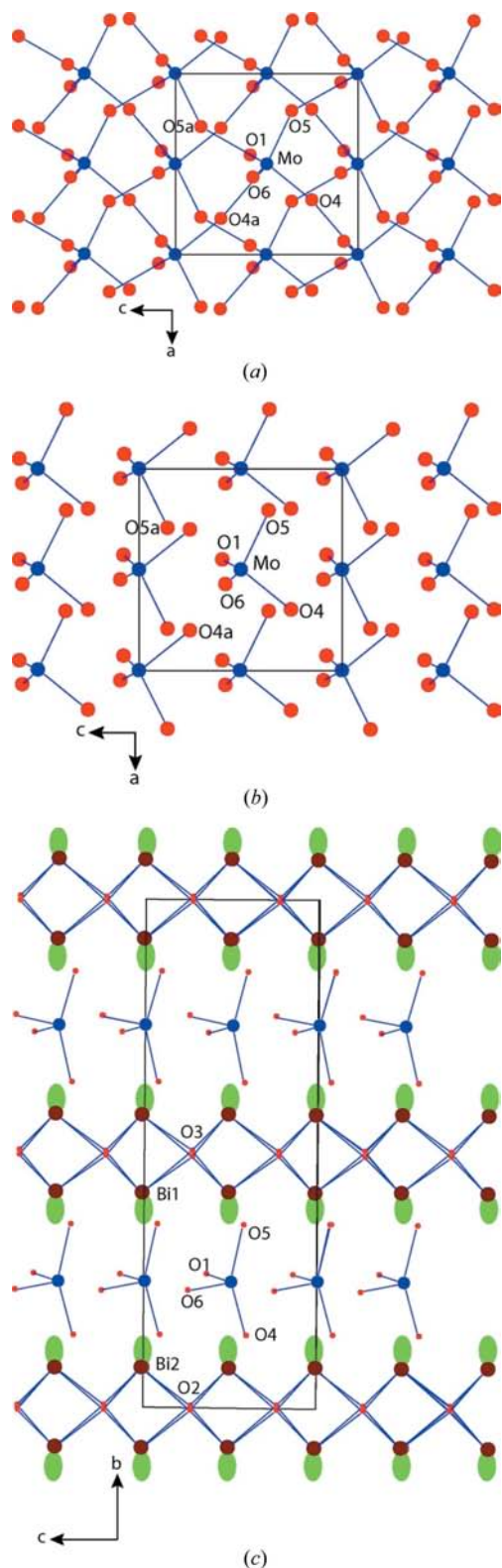


Figure 5
 (a) The pseudo-perovskite [MoO₄] layer of [MoO₆] octahedra in Bi₂MoO₆ koechlinite. The O atoms are depicted in red and Mo in blue. The unit cell is indicated in black. (b) The pseudo-perovskite [MoO₄] layer in Bi₂MoO₆ koechlinite without plotting the two longest bonds Mo–O_{4a} = 2.18 Å and Mo–O_{5a} = 2.30 Å. (c) Structure model of Bi₂MoO₆ koechlinite. The O atoms are depicted in red, Mo in blue and Bi in brown. The lone pairs are sketched in green. The unit cell is indicated in black.

cationic model atomic coordinates are collected in Table 1.

Image calculations for this model at different thicknesses and defoci are deposited in the supplementary material¹ and demonstrate that the contribution of the O atoms to the image contrast is negligible. From these simulations we assume that the large ‘white blobs’ observed in the HRTEM image can be associated with the central channel that lies in-between the two rows of Bi atoms in the model proposed. In the center of Fig. 3(a) the simulation corresponding to this cationic model with a thickness of 10 nm and a defocus of –100 nm is inserted. Notice the very good agreement between the experimental and simulated HRTEM images. This image interpretation will be used to elucidate the cationic frame structure of the higher *n*-term phases.

We have also calculated the SAED pattern for this cationic model along the short axis *b*, *i.e.* in the orientation characteristic for these phases, see Fig. 4(a). This simulated electron diffraction pattern fits very well with the experimental one shown in Fig. 2. The X-ray diffraction pattern calculated for this cationic model, see the supplementary material, agrees well with the experimental pattern shown in Fig. 4(d) of Vila *et al.* (2007).

All these results clearly demonstrate that in this Bi–Mo–O family of compounds the cationic model can also be compared with electron microscopy and powder X-ray diffraction experiments, in spite of the fact that we have neglected to include the O atoms in the structure. They do affect the intensity of some reflections, but the general agreement validates this cationic model. This procedure is therefore valid to elucidate the heavy atom framework from the HRTEM images of the structures of the other members of this family of compounds.

3.2. The *n* = 4 phase, Bi₁₂Mo₄O₃₀

The X-ray powder pattern of the *n* = 4 sample, Bi₁₂Mo₄O₃₀, with a Bi/Mo ratio of 3.0, was indexed by Vila *et al.* (2005, 2007) in space groups *Pa* and *P2/a* with unit-cell parameters *a* = 29.0674 (4), *b* = 5.64795 (7) and *c* = 8.6620 (1) Å and β = 97.979 (1)°. However, the structural relationship proposed by Vila *et al.* (2007) in Fig. 8 suggests that the unit cells of phases *n* = 4 and *n* = 6 should be primitive and halved in *a*. The electron diffraction results confirm this suspicion.

The HRTEM images of this phase, Fig. 3(b), show a contrast that is very similar to that of the Bi₁₀Mo₃O₂₄ phase HRTEM images, consisting of strings of large ‘white blobs’ running in a zigzag arrangement along *a*, which are caused by ribbons of {MoO₄} tetrahedra. Nevertheless, the length of these strings is longer than in the former case, corresponding to strings of four tetrahedra. Notice that the crystals of this phase seem to be more stable under the electron beam and, consequently, we have been able to obtain HRTEM images of a thin and clean crystal edge. A cationic model has been developed for this phase, see Fig. 1(b) and Table 2, based on the cationic struc-

¹ Supplementary data for this paper are available from the IUCr electronic archives (Reference: WH5006). Services for accessing these data are described at the back of the journal.

ture model of $\text{Bi}_{10}\text{Mo}_3\text{O}_{24}$. The model consists of ribbons of four Mo atoms which are inserted within a $\delta\text{-Bi}_2\text{O}_3$ matrix of bismuths. The space group $P2_1$ fits well with the cationic model proposed using the HRTEM images, although the oxygen sublattice could change the symmetry. The simulated HRTEM image corresponding to this cationic model has been calculated for a thickness of 5 nm and a defocus of -60 nm and fits very well with the experimental HRTEM image (see the image calculation in Fig. 3*b*). The calculated SAED (Fig. 4*b*) and powder diffraction patterns (see supplementary material, Fig. 4) fit very well with the experimental patterns shown in Fig. 6*b*) and Fig. 4*c*) of Vila *et al.* (2007).

3.3. The $n = 5$ phase, $\text{Bi}_{14}\text{Mo}_5\text{O}_{36}$

The $n = 5$ phase ($\text{Bi}_{14}\text{Mo}_5\text{O}_{36}$) with a Bi/Mo ratio of 2.80 and unit-cell parameters $a = 34.476$ (2), $b = 5.6414$ (3) and $c = 8.6433$ (4) Å, and $\beta = 99.690$ (5)° shows the same C-centered symmetry as the $n = 3$ member, *i.e.* $\text{Bi}_{10}\text{Mo}_3\text{O}_{24}$. The HRTEM image is shown in Fig. 3*c*). Notice that the contrast is reversed with respect to the observed image in the previous two phases. The image is closer to the Scherzer defocus which is easier to interpret by identifying the big ‘black blobs’ of the image as Mo atoms. Considering the similarities between the HRTEM images of these phases (*cf.* the images of Figs. 3*a*, *b* and *c*) it is reasonable to conclude that the $\{\text{MoO}_4\}$ tetrahedra ribbons now consist of five units. The proposed cationic model for this phase is described in Table 3 and Fig. 1*c*). Again, the HRTEM image is simulated for this model at different thicknesses and defoci and the best-fitting one, corresponding to a thickness of 5 nm and a defocus of -30 nm, is inserted in Fig. 3*c*) with good agreement.

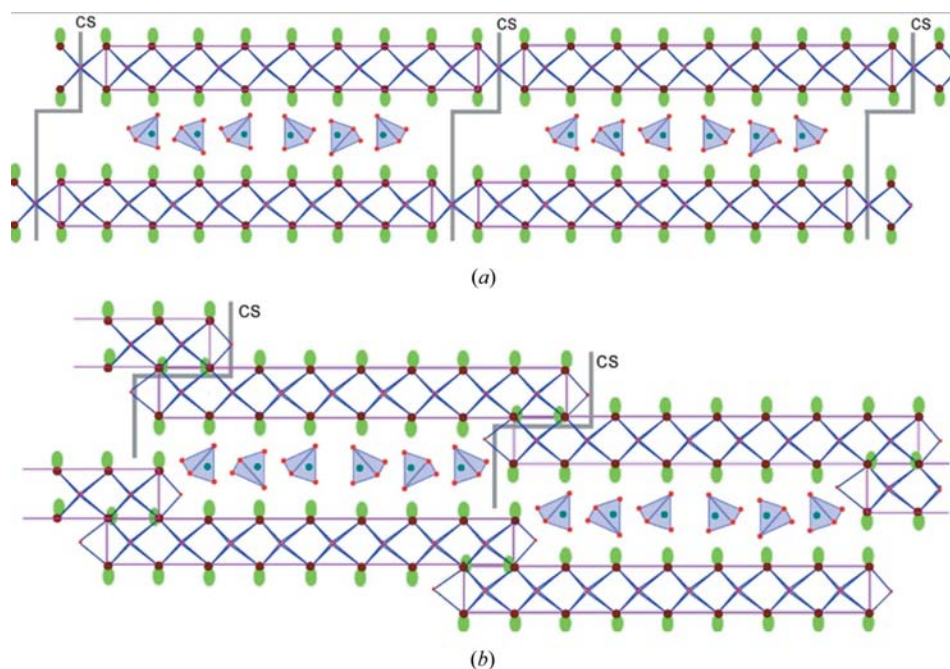


Figure 6 Crystallographic shear (CS) operation applied to Bi_2Mo_6 every three $\{\text{MoO}_4\}$ tetrahedra (*a*) give rise to the $\text{Bi}_{16}\text{Mo}_6\text{O}_{42}$ structure (*b*). Grey lines indicate the CS operation.

Table 4

Cationic structural model proposed for $\text{Bi}_{16}\text{Mo}_6\text{O}_{42}$.

$a = 19.98$ (2), $b = 5.632$ (4) and $c = 8.634$ (4) Å, $\beta = 101.02$ (2)° (at room temperature); space group $P2_1$.

	<i>x</i>	<i>y</i>	<i>z</i>
Mo1	41/44	0.0	1/44
Mo2	35/44	0.5	2/44
Mo3	29/44	0.0	3/44
Bi1	23/44	0.5	4/44
Bi2	17/44	0.0	5/44
Bi3	11/44	0.5	6/44
Bi4	5/44	0.0	7/44
Bi5	43/44	0.5	8/44
Bi6	37/44	0.0	9/44
Bi7	31/44	0.5	10/44
Bi8	25/44	0.0	11/44

The corresponding simulated SAED and PXRD patterns are collected in Fig. 4*c*) and the supplementary material (Fig. 5), and they correspond well to those of $\text{Bi}_{14}\text{Mo}_5\text{O}_{36}$ shown by Vila *et al.* (2007).

3.4. The $n = 6$ phase, $\text{Bi}_{16}\text{Mo}_6\text{O}_{42}$

Finally, the $n = 6$ phase ($\text{Bi}_{16}\text{Mo}_6\text{O}_{42}$) is similar to the $n = 4$ member ($\text{Bi}_{12}\text{Mo}_4\text{O}_{30}$) of the $\text{Bi}_{2(n+2)}\text{Mo}_n\text{O}_{6(n+1)}$ family of compounds. This phase is more unstable than the preceding ones, as already confirmed by Vila *et al.* (2007), where the low conductivity values of this phase are attributed to its low thermal stability. This instability dramatically affects the HRTEM experiments since this phase is even more quickly damaged by the electron beam than the previous ones. Nonetheless, reasonable HRTEM images could be obtained.

The cationic model therefore consists of strings of six $\{\text{MoO}_4\}$ tetrahedra inserted in the $\delta\text{-Bi}_2\text{O}_3$ matrix, see the cationic structural model shown in Fig. 3*d*), corresponding to the atomic coordinates in Table 4. The image simulation in Fig. 3*d*) has been calculated for this cationic model and fits well enough with the experimental image, indicating that the structure model proposed is very close to the real structure of this phase.

4. Structural discussion

From these results it can be envisaged that the new family of compounds described are structurally closely related. From the general family formula $\text{Bi}_{2(n+2)}\text{Mo}_n\text{O}_{6(n+1)}$, we can deduce that the $n = 0$

member would correspond to the stoichiometry Bi_2O_3 , the $n = 1$ member to $\text{Bi}_6\text{MoO}_{12}$ and the $n = 2$ member to $\text{Bi}_8\text{Mo}_2\text{O}_{18}$. So far this has not been described for any of these members with a similar structure. However, it is important to note that the end member of this series, $n = \infty$, is the $\gamma(\text{L})\text{Bi}_2\text{MoO}_6$ polymorph (koechlinite; van den Elzen & Rieck, 1973), which shows an Aurivillius-type layered structure, *i.e.* consists of a

$[\text{MoO}_4]^{2-}$ layer of perovskite-type $\{\text{MoO}_6\}$ corner-connected octahedra, periodically stacked with $[\text{Bi}_2\text{O}_2]^{2+}$ layers.

Nevertheless, although at first sight this phase does not seem to be the end member of the series structurally due to the perovskite layer, a closer look at this layer leads to a different conclusion. Notice that just by moving the Mo atoms from the center of the octahedra towards the center of one of

the equatorial edges we can transform the perovskite layer into a layer of isolated tetrahedra. In Fig. 5(a) the perovskite layer is plotted as a layer of $\{\text{MoO}_6\}$ corner-connected octahedra. However, the $\{\text{MoO}_6\}$ octahedra are far from ideal since they exhibit two different classes of Mo–O distance, one with four bond lengths of *ca.* 1.75 Å and another with bond lengths of 2.18 and 2.30 Å. If the same layer is depicted without the two longest Mo–O distances of 2.18 and 2.30 Å, see Figs. 5(b) and (c), then the layer can be described as a layer composed of unconnected $\{\text{MoO}_4\}$ tetrahedra, similar to La_2MoO_6 and the refined structure of $\text{Bi}_{10}\text{Mo}_3\text{O}_{24}$. Therefore, a clear structural link can be established between koechlinite and the $\text{Bi}_{2(n+2)}\text{Mo}_n\text{O}_{6(n+1)}$ family of compounds. Actually, the whole family can be described as the result of a crystallographic shear (CS) operation in Aurivillius-type structures, starting from the koechlinite (Bi_2MoO_6 , $n = \infty$) phase. We can describe the CS operation as the result of adding Bi_2O_3 to the $(\text{Bi}_2\text{O}_2)^{2+}$ layer in order to attain the different compositions of the different members of the $\text{Bi}_{2(n+2)}\text{Mo}_n\text{O}_{6(n+1)}$ family. As we do this, we can consider that the $(\text{Bi}_2\text{O}_2)^{2+}$ layer is stretched, as shown in Fig. 6(a), leaving unstable voids in the $[\text{MoO}_4]^{2-}$ perovskite layer. The structure then collapses, giving rise to a crystallographic shear. When we apply this operation to every six $\{\text{MoO}_4\}$ tetrahedra we obtain the structure model for the $n = 6$ member of the family, *i.e.* $\text{Bi}_{16}\text{Mo}_6\text{O}_{42}$, see Fig. 6(b).

This mechanism can be extended to the $n = 5$ ($\text{Bi}_{14}\text{Mo}_5\text{O}_{36}$), $n = 4$ ($\text{Bi}_{12}\text{Mo}_4\text{O}_{30}$) and $n = 3$ ($\text{Bi}_{10}\text{Mo}_3\text{O}_{24}$) phase members of this family leaving rectangular tunnels

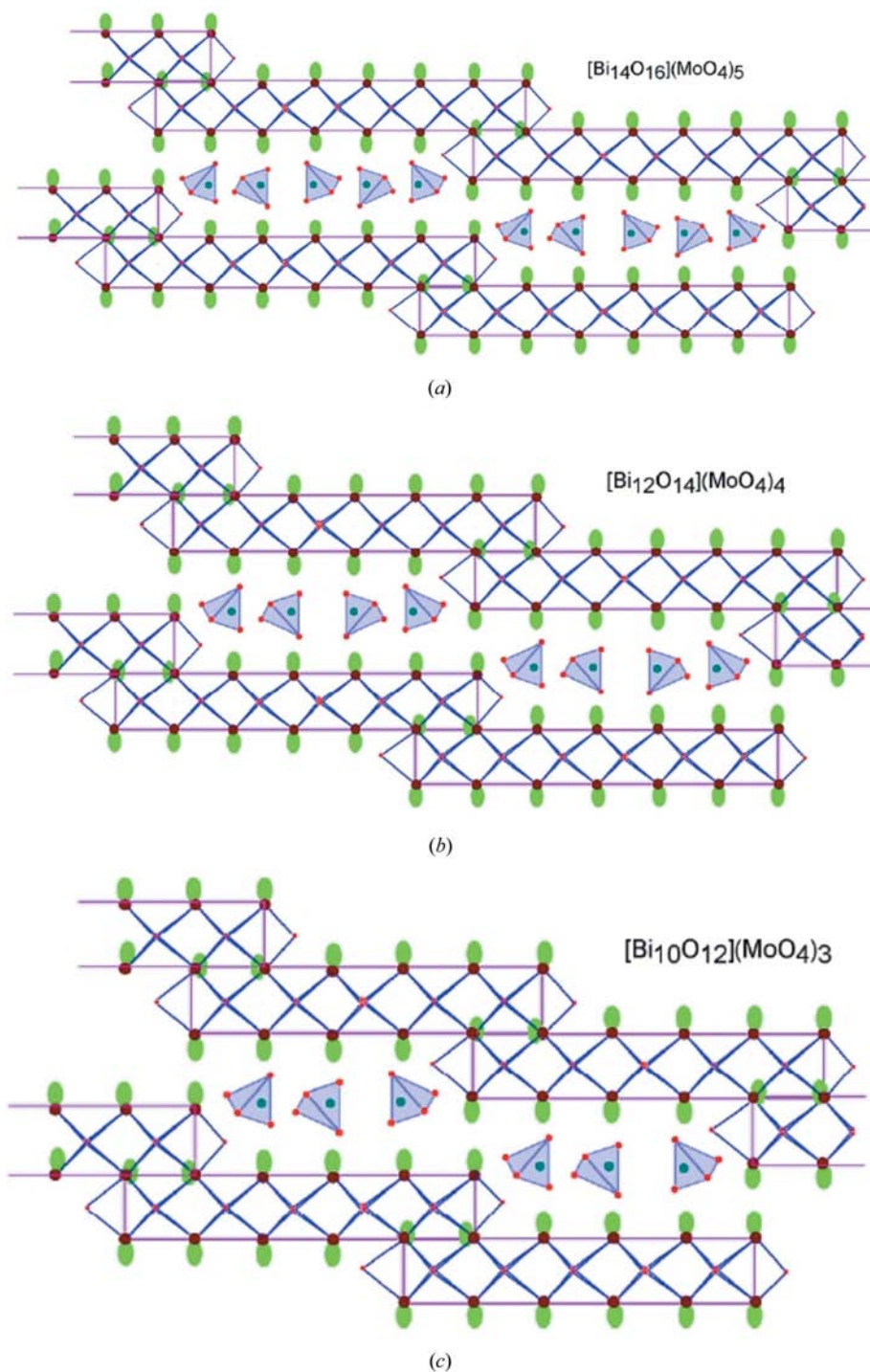


Figure 7

Schematic atomic models of phases (a) $\text{Bi}_{14}\text{Mo}_5\text{O}_{36}$, (b) $\text{Bi}_{12}\text{Mo}_4\text{O}_{30}$ and (c) $\text{Bi}_{10}\text{Mo}_3\text{O}_{24}$. Mo atoms are depicted in blue, Bi in dark red, O atoms in bright red and lone pairs of electrons in green.

filled with five, four and three $\{\text{MoO}_4\}$ tetrahedra surrounded by bismuth lone pairs. Fig. 7 shows how the CS operation applied to the Bi_2MoO_6 structure every five, four and three Mo atoms leads to the $n = 5$, $n = 4$ and $n = 3$ members of the family. After this operation a $[\text{Bi}_{10}\text{O}_{12}]_n$ layer is obtained leaving rectangular tunnels filled with groups of three $\{\text{MoO}_4\}$ tetrahedra which are reorganized in this space bordered by lone pairs.

In MoO_3 the molybdenum is inside an octahedron so distorted that it is reasonable, considering the Mo–O bond-length distribution, to consider that Mo has CN = 4. In La_2MoO_6 the molybdenum is located in an almost perfect tetrahedron (Xue *et al.*, 1995), so we consider this to be the molybdenum(VI) preferred coordination. However, in Bi_2MoO_6 the Mo atom is inside a distorted octahedron, but why? The structure is the same as in La_2MoO_6 , but there is a marked difference. Lanthanum does not have lone pairs of electrons pointing towards the $[\text{MoO}_4]_n$ layer, as does bismuth. Thus, somehow it is the lone pair that perturbs the tetrahedral coordination of Mo atoms. It seems clear that the bismuth lone pair affects the regular distribution of O atoms around the Mo atoms. The mechanism of such a distortion is beyond the purpose of this paper. In any case, following this line of argument, we can predict that as the n value increases, the Mo atoms in the center of the $[\text{MoO}_4]_n$ ribbons will have similar surroundings as in Bi_2MoO_6 and the Mo atoms will be moving inside the oxygen octahedra.

5. Conclusions

In the present work transmission electron microscopy has been used to elucidate the cationic framework structure of a whole new family of $\text{Bi}_{2(n+2)}\text{Mo}_n\text{O}_{6(n+1)}$ phases with four members for $n = 3, 4, 5$ and 6 , characterized by fluorite-type superstructures. All these phases are structurally related and consist of a basic framework of $\delta\text{-Bi}_2\text{O}_3$, with a fluorite-type structure, which shows ribbons of $\{\text{MoO}_4\}$ tetrahedra which are infinite along b , regularly spaced along c , and with a variable length along a . It is along the latter axis that they show the main difference since the different phases show different lengths of the Mo ribbons along this direction, ranging from ribbons of three $\{\text{MoO}_4\}$ tetrahedra for $n = 3$, four for $n = 4$, five for $n = 5$ and six for $n = 6$ phases. These $\{\text{MoO}_4\}$ tetrahedra are considered to be isolated, *i.e.* without sharing either corners or edges as in the $[\text{Bi}_{12}\text{O}_{14}]$ columnar structural-type phase $\text{Bi}[\text{Bi}_{12}\text{O}_{14}][\text{MoO}_4]_4[\text{VO}_4]$ (Enjalbert *et al.*, 1997). Family members with $n > 6$ have been sought and not found, and the nominal compositions of intermediates between consecutive n members, looking for intergrowths with more complicated sequences of $\{\text{MoO}_4\}$ tetrahedral ribbons, have only yielded a mixture of phases.

The generation of all these phases can be described by applying a crystallographic shear operation to a starting Aurivillius-type Bi_2MoO_6 phase ($n = \infty$).

The authors want to thank the Spanish MICINN (MAT2007-61884 project) for financial support. JHV is grateful for funding through the Ramón y Cajal program.

References

- Agarwal, D. D., Madhok, K. L. & Goswami, H. S. (1994). *React. Kinet. Catal. Lett.* **52**, 225–232.
- Bastide, B., Enjalbert, R., Salles, Ph. & Galy, J. (2003). *Solid State Ionics*, **158**, 351–358.
- Bégué, P., Rojo, J. M., Enjalbert, R., Galy, J. & Castro, A. (1998). *Solid State Ionics*, **112**, 275–280.
- Bégué, P., Rojo, J. M., Iglesias, J. E. & Castro, A. (2002). *J. Solid State Chem.* **166**, 7–14.
- Brazdil, J. F., Suresh, D. D. & Grasselli, R. K. (1980). *J. Catal.* **66**, 347–367.
- Buttrey, D. J., Jefferson, D. A. & Thomas, J. M. (1986a). *Mater. Res. Bull.* **21**, 739–744.
- Buttrey, D. J., Jefferson, D. A. & Thomas, J. M. (1986b). *Philos. Mag. A*, **53**, 897–906.
- Buttrey, D. J., Vogt, T., Wildgruber, U. & Robinson, W. R. (1994). *J. Solid State Chem.* **111**, 118–127.
- Buttrey, D. J., Vogt, T., Yap, G. P. A. & Rheingold, A. L. (1997). *Mater. Res. Bull.* **32**, 947–963.
- Castro, A., Aguado, E., Rojo, J. M., Herrero, P., Enjalbert, R. & Galy, J. (1998). *Mater. Res. Bull.* **33**, 31–41.
- Castro, A. & Palem, D. (2002). *J. Mater. Chem.* **12**, 2774–2780.
- Chen, H.-Y. & Sleight, A. W. (1986). *J. Solid State Chem.* **63**, 70–75.
- Crumpton, T. E., Francesconi, M. G. & Greaves, C. (2003). *J. Solid State Chem.* **175**, 197–206.
- Duc, F., Rozier, P., Millet, P. & Galy, J. (2004). *Solid State Sci.* **6**, 897–905.
- Elzen, A. F. van den & Rieck, G. D. (1973). *Acta Cryst.* **B29**, 2436–2438.
- Enjalbert, R., Hasselmann, G. & Galy, J. (1997). *J. Solid State Chem.* **131**, 236–245.
- Galvan, D. H., Fuentes, S., Avalos-Borja, M., Cota-Araiza, L., Early, E. A., Maple, M. B. & Cruz-Reyes, J. (1993). *J. Phys. Condens. Matter*, **5**, A217–A218.
- Galy, J., Hernández-Velasco, J., Landa-Cánovas, A. R., Vila, E. & Castro, A. (2009). *J. Solid State Chem.* **182**, 1177–1187.
- Galy, J., Salles, Ph., Rozier, P. & Castro, A. (2006). *Solid State Ionics*, **177**, 2897–2902.
- Grins, J., Esmailzadeh, S. & Hull, S. (2002). *J. Solid State Chem.* **163**, 144–150.
- Holmes, L., Peng, L., Heinmaa, I., O'Dell, L. A., Smith, M. E., Vannier, R. N. & Grey, C. P. (2008). *Chem. Mater.* **20**, 3638–3648.
- Kohlmüller, R. & Badaud, J. P. (1969). *Bull. Soc. Chim. France*, **10**, 3434.
- Ling, C. D. (1999). *J. Solid State Chem.* **148**, 380–405.
- Ling, C. D., Withers, R. L., Schmid, S. & Thompson, J. G. (1998). *J. Solid State Chem.* **137**, 42–61.
- Miida, R. & Tanaka, M. (1990). *Jpn. J. Appl. Phys.* **29**, 1132–1138.
- Muktha, B. & Guru Row, T. N. (2007). *Struct. Chem.* **18**, 195–202.
- Pirnat, U., Valant, M., Jancar, B. & Suvorov, D. (2005). *Chem. Mater.* **17**, 5155–5160.
- Roth, R. S. & Waring, T. L. (1962). *J. Res. Natl. Bur. Stand. A*, **66**, 451–463.
- Spinolo, G. & Tomasi, C. (1997). *Powder Diffr.* **12**, 16–19.
- Theobald, F., Laarif, A. & Hewat, A. W. (1985). *Mater. Res. Bull.* **20**, 653–665.
- Vallidor, M., Esmailzadeh, S., Pay-Gomez, C. & Grins, J. (2000). *J. Solid State Chem.* **152**, 573–576.
- Vannier, R. N., Abraham, F., Nowogrocki, G. & Mairesse, G. (1999). *J. Solid State Chem.* **142**, 294–304.
- Vannier, R. N., Danzé, S., Nowogrocki, G., Huvé, M. & Mairesse, G. (2000). *Solid State Ionics*, **136–137**, 51–59.

- Vera, C. M. C. & Aragón, R. (2008). *J. Solid State Chem.* **181**, 1075–1079.
- Vila, E., Iglesias, J. E., Galy, J. & Castro, A. (2005). *Solid State Sci.* **7**, 1369–1376.
- Vila, E., Landa-Canovas, A. R., Galy, J., Iglesias, J. E. & Castro, A. (2007). *J. Solid State Chem.* **180**, 661–669.
- Vila, E., Rojo, J. M., Iglesias, J. E. & Castro, A. (2004). *Chem. Mater.* **16**, 1732–1739.
- Xue, J. S., Antonio, M. R. & Soderholm, L. (1995). *Chem. Mater.* **7**, 333–340.
- Zhou, W., Jefferson, D. A., Alario-Franco, M. A. & Thomas, J. M. (1987). *J. Phys. Chem.* **91**, 512–514.